Hydrodynamic interactions between two semiflexible inextensible filaments in Stokes flow

Y.-N. Young
Department of Mathematical Sciences, New Jersey Institute of Technology, Newark, New Jersey 07102, USA
(Received 17 November 2008; revised manuscript received 10 February 2009; published 20 April 2009)

Hydrodynamic interactions between two semiflexible inextensible filaments are shown to have a significant impact on filament buckling and their subsequent motion in Stokesian fluids. In linear shear flow, hydrodynamic interactions lead to filament shear dispersion that depends on the filament aspect ratio and the initial filament separation. In linear extensional flow, hydrodynamic interactions lead to complex filament dynamics around the stagnation point. These results suggest that hydrodynamic interactions need to be taken into account to determine the self-diffusion of non-Brownian semiflexible filaments in a cellular flow [Y.-N. Young and M. J. Shelley, Phys. Rev. Lett. **99**, 058303 (2007)].

DOI: 10.1103/PhysRevE.79.046317 PACS number(s): 47.57.−s, 46.32.+x, 47.57.E−, 47.35.−i

I. INTRODUCTION

Hydrodynamic interactions (HIs) between rigid particles have significant effects on the macroscopic mechanical properties of their suspension. For example, hydrodynamic interactions between rigid fibers are crucial to the concentration instability observed in sedimenting fiber suspensions [1]. For suspension of rigid active fibers such as actuated swimmers, hydrodynamic interactions are found to help order the swimmers over short length scales, and have a significant impact on the mean swimming speed [2–4]. Recently hydrodynamic interactions between rigid spheres in a thin channel are found to lead to novel nonlinear pattern formation and dynamics [5].

When combined with particle deformability, hydrodynamic interactions affect both the individual particle shape dynamics and the macroscopic properties of the suspension. An example is the non-Brownian viscous drop suspensions in shear flow. Loewenberg and Hinch [6] used the boundary integral formulation to numerically investigate the effects of hydrodynamic interactions on dilute suspension of viscous drops in shear flow, and concluded that the hydrodynamic interaction and drop deformation conspire to suppress drop breakup during the collision process. The self-diffusion coefficients of the non-Brownian drops in a dilute sheared emulsion are obtained from trajectories of different collision processes between a pair of viscous drops, and are found to be anisotropic and dependent on the viscosity ratio and the shear rate. As a result, the mixing efficiency of drop suspensions is affected by the hydrodynamic interactions between deformable drops. Another example of hydrodynamic interactions' effects on macroscopic properties of soft particle suspension is the semidilute vesicle suspension in a shear flow. Hydrodynamic interactions between vesicles give rise to strong fluctuations in vesicle shape and inclination angle [7]. The macroscopic viscosity of vesicle suspension is found to depend nonmonotonically on the viscosity ratio between the inner and outer fluids of the vesicles.

The hydrodynamics of semiflexible inextensible filaments in viscous fluids has gained interest due to their close relevance in biofluids and microfluidics. Many semiflexible biopolymers, such as DNA, cilia, and flagella, are virtually inextensible, and their dynamics in viscous fluids plays a central role in their motion [8–11]. New advances in microfabrication and micromanipulation enable direct interaction with semiflexible biopolymers in simplified *in vitro* environments, and stimulate more interest in investigation of the dynamics of flexible biofilaments. For example, optical tweezers are employed to periodically oscillate actin filaments connected to micron-sized beads, in order to devise an artificial "one-armed swimmer" [12]. Polymer-linked magnetic beads are used to design artificial swimmers that can be controlled in a magnetic field [13]. This novel design enables an easier control of the filaments through magnetic fields and has allowed quantitative measurements of the physical properties of the chains, such as their bending stiffness. Similar methodologies are applied to induce properties of the linker molecules [14] or the affinity of chemical contacts between polymer and particle coating from video microscopy [15]. Semiflexible actin filaments are now used as nanocargos in microfluidic devices for directed transport on chemically patterned surfaces [16]. Fabrication of synthetic ciliary arrays and technological applications of artificial swimmers are also new possibilities to be explored.

The aspect ratio (radius to length) of most semiflexible inextensible biopolymers ranges from 10^{-5} to 10^{-1}. The extreme aspect ratio justifies the slender-body formulation in Stokes flow, a very viscous flow with essentially zero Reynolds number. A significant amount of work has been devoted to the studies of a single elastic inextensible filament in slender-body formulation [8,17–19]. Recently the hydrodynamics of multiple filaments in Stokes flow has been investigated. Tornberg and Shelley [20] used the nonlocal slender-body model to numerically simulate dynamics of multiple (up to 25) interacting filaments in a background oscillating shear flow. Llopis *et al.* [21] investigated the effects of hydrodynamic interactions on the sedimentation of a pair of inextensible filaments using the bead model. Dillon *et al.* [10] examined multiciliary interaction in a mucus layer using the immersed boundary method.

While sufficient progress has been made to understand the complex hydrodynamics of elastic filaments, quantitative detail of interacting semiflexible filament dynamics remains incomplete. For example, how does a semiflexible filament buckle under hydrodynamic interactions with other filaments in the neighborhood? Do the hydrodynamic interactions between two buckling filaments in shear flow cause filament

self-diffusion as in the case of viscous drop suspension? How will HIs between non-Brownian elastic filaments in cellular flow affect the diffusive transport due to filament buckling around the stagnation points [22]? To gain fundamental insights into the complex interplay between filament self-diffusion, filament deformation, and hydrodynamic interactions, it is useful to consider the dynamics of a pair of semiflexible filaments in simple flows.

We will examine the effects of HIs between a pair of filaments in configurations where a single elastic inextensible filament is known to exhibit buckling instability [20,22]. We will examine how HIs induce differences in the buckling dynamics and the subsequent filament motion. For a single semiflexible filament subject to a body force, different filament shapes and dynamics are found as a result of both the nonlocal HIs and elasticity [23]. For a pair of sedimenting filaments, filament elasticity and nonlocal HIs conspire to cause interesting filament shapes and cooperative filament motion under gravity [21]. Our goal is to elucidate how such combination affects buckling of a pair of semiflexible filaments in linear flows.

In particular, we will focus on simulating the buckling dynamics of a pair of interacting filaments in two prototypical linear flows: planar shear flow and planar extensional flow. (1) Filaments in the plane of shear flow (in the x direction) experience compressive stress only when rotating toward the cross-shear axis (y axis). For these simulations, the initial conditions are chosen to elucidate the generic trend of the HI effects on filament buckling dynamics in shear flow (explained in detail in Sec. III). (2) Filaments in linear extensional flow experience compression when they move toward the stagnation point. Two filaments parallel to the compressional axis are initially placed on the opposite sides of the stagnation point. As explained in Sec. IV these initial configurations allow us to gain quantitative insights into the roles of HIs in buckling of two interacting filaments in terms of filament shape parameter and effective viscosity.

In our formulation Brownian forces (kT/L) are neglected relative to drag and elastic forces ($\mu\dot{\gamma}L^2$ and Yr^4/L^2, respectively; Y is the Young modulus). This is because predominance of drag force requires $L \gg L_1 = (kT/\mu\dot{\gamma})^{1/3}$, which for water and $\dot{\gamma}=1\ \mathrm{s}^{-1}$ gives $L_1 \sim 1\ \mu$m. Predominance of elastic forces requires $L \gg /_2 = (kT/Y\epsilon^4)^{1/3}$, which for aspect ratio $\epsilon = r/L = 10^{-3}$ and $Y=1$ GPa also yields $L_2 \sim 1\ \mu$m. Thus we conclude that Brownian forces can be reasonably neglected for filaments of length larger than $1\ \mu$m in water with $\dot{\gamma}=1\ \mathrm{s}^{-1}$ at room temperature.

The rest of the paper is organized as follows. In Sec. II the slender-body formulation for interacting inextensible elastic filaments immersed in Stokes flow is presented. The Hasimoto transformation is utilized to convert the integro-differential slender-body equations to a system of equations for the complex curvature of the filament centerlines [24]. The resultant system is numerically integrated using the numerical scheme summarized in Sec. II. We quantify HI effects on the buckling dynamics of two filaments in time-independent, two-dimensional linear flows. In Sec. III we summarize results from simulating a pair of semiflexible filaments immersed in the plane of linear shear flow. In particular we focus on how HIs induce different buckling dynamics and cause filament dispersion in shear flow. In Sec. IV we summarize results from simulating a pair of semiflexible filaments moving toward each other around the stagnation point in extensional flow. HIs lead to different dynamics of filaments in straining flow, and simulation data provide quantitative description of different filament dynamics. We also discuss how the nonlocal slender-body formulation needs to be modified to enforce the noncontact, noncrossing conditions for two filaments undergoing buckling instability. Finally in Sec. V we present conclusions and discuss ongoing work.

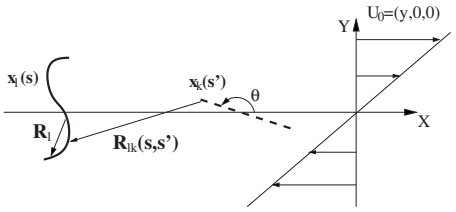

FIG. 1. Illustration of two filaments in a planar shear flow $\mathbf{U}_0$. $\mathbf{x}_l(s)$ (left filament, thick solid line) and $\mathbf{x}_k(s)$ (right filament, thick dashed line) are the filament centerline positions, and θ is the filament angle with respect to the x axis.

II. FORMULATION

We consider interacting semiflexible inextensible slender filaments immersed in a viscous fluid. Ignoring external forcing (such as gravity) and focusing on low-Reynolds-number flows (no inertia effects), the Stokes equations are appropriate to describe the dynamics of the system sketched in Fig. 1. For very slender filaments the governing Stokes equations can be reduced to a system of nonlinear, nonlocal integro-differential equations as in [20]. Immersed in a background flow with a characteristic time $\dot{\gamma}^{-1}$, all filaments are assumed to be of equal length L with the same bending rigidity E and filament aspect ratio ϵ [hence the same coefficient $c \equiv \log(\epsilon^2 e)$]. The equations are rendered dimensionless by using L for length unit, $\dot{\gamma}^{-1}$ for time unit, and E/L^2 for force unit. In the slender-body formulation, the lth filament is described by its centerline position $\mathbf{x}_l$ parametrized by arc length $s \in [0,1]$. Throughout the paper the subscript s denotes the derivative with respect to arc length. The dynamics of the lth filament interacting with other filaments in a background flow $\mathbf{U}_0$ is given by the following dimensionless equations [20]:

$$\frac{8\pi\mu\dot{\gamma}L^4}{E}\left(\frac{\partial \mathbf{x}_l}{\partial t} - \mathbf{U}_0(\mathbf{x}_l)\right) = [(-c+2)\mathbf{I} + (-2-c)\mathbf{x}_{ls}\mathbf{x}_{ls}]\mathbf{f}_l - K_l - \sum_{k\neq l}^{M} V_{lk}, \tag{1}$$

with μ as the fluid viscosity, $\mathbf{I}$ as the identity tensor, and $\mathbf{x}_{ls}\mathbf{x}_{ls}$ as a dyadic product. The force-free boundary conditions give $\mathbf{x}_{lss}=\mathbf{x}_{lsss}=0$ at filament end points. The line force density $\mathbf{f}_l$ consists of a bending force and a tensile force that enforces filament inextensibility,

$$\mathbf{f}_l(s) = \mathbf{x}_{lssss} - [T_l(s)\mathbf{x}_{ls}]_s. \tag{2}$$

The self-hydrodynamic interaction K_l is given by the finite-part integral

$$K_l = \int_0^1 \left(\frac{\mathbf{I} + \hat{\mathbf{R}}_l(s,s')\hat{\mathbf{R}}_l(s,s')}{|\mathbf{R}_l(s,s')|}\mathbf{f}_l(s') - \frac{\mathbf{I} + \mathbf{x}_{ls}(s)\mathbf{x}_{ls}(s)}{|s-s'|}\mathbf{f}_l(s) \right) ds', \tag{3}$$

and the hydrodynamic interactions between the lth and kth filaments are

$$V_{lk} = \int_0^1 \frac{\mathbf{I} + \hat{\mathbf{R}}_{lk}(s,s')\hat{\mathbf{R}}_{lk}(s,s')}{|\mathbf{R}_{lk}(s,s')|}\mathbf{f}_k(s')ds'. \tag{4}$$

In the above integrals $\mathbf{R}_l(s,s') = \mathbf{x}_l(s) - \mathbf{x}_l(s')$ and $\mathbf{R}_{lk}(s,s') = \mathbf{x}_l(s) - \mathbf{x}_k(s')$ as sketched in Fig. 1, and $\hat{\mathbf{R}}_l(s,s') = \mathbf{R}_l(s,s')/|\mathbf{R}_l(s,s')|$ and $\hat{\mathbf{R}}_{lk}(s,s') = \mathbf{R}_{lk}(s,s')/|\mathbf{R}_{lk}(s,s')|$.

The inextensibility condition of the lth filament $\mathbf{x}_{ls}\cdot\mathbf{x}_{ls} = 1$ gives the following equation for the line tension:

$$2cT_{lss} + (2-c)(\mathbf{x}_{lss}\cdot\mathbf{x}_{lss})T_l = \mathbf{x}_{ls}\cdot\frac{\partial}{\partial s}\left(\frac{8\pi\mu\dot{\gamma}L^4}{E}\mathbf{U}_0(\mathbf{x}_l) - K_l - \sum_{k\neq l}^{M} V_{lk} \right) + (2-7c)(\mathbf{x}_{lss}\cdot\mathbf{x}_{lsss}) - 6c(\mathbf{x}_{lsss}\cdot\mathbf{x}_{lsss}), \tag{5}$$

subject to the force-free boundary condition $T_l(s=0,1)=0$. The above slender-body equations for interacting filaments in Stokes flow were numerically investigated by Tornberg and Shelley [20]. The authors regularized the finite-part interaction integral and constructed a numerical method to successfully avoid severe stability constraint due to the bending force. Using this numerical method, the authors were able to simulate the collective dynamics of 25 interacting elastic filaments in a shear flow.

In the present work we apply the Hasimoto transformation [18,24,25] to the above slender-body equations with hydrodynamic interactions. Instead of the centerline position for the lth filament, the filament complex curvature $\psi_l \equiv \kappa_l e^{i\phi_l}$ is the main dynamical variable, and $\tau_l \equiv \partial\phi_l/\partial s$ is the corresponding torsion. In this formulation the natural coordinate system is the unit tangent ($\hat{\mathbf{t}}_l$), normal ($\hat{\mathbf{n}}_l$), and binormal ($\hat{\mathbf{b}}_l$) vectors along the filament centerline. The slender-body equations are recast in terms of complex curvature ψ_l and the three unit vectors,

$$\frac{8\pi\mu\dot{\gamma}L^4}{E}\frac{\partial\psi_l}{\partial t} = (\partial_{ss} + |\psi_l|^2)\Gamma_l + G_l, \tag{6}$$

$$\Gamma_l \equiv (U_l + iV_l)e^{i\phi_l}, \tag{7}$$

$$G_l \equiv \psi_l \,\mathrm{Im}\int ds'\,\psi_{ls'}\Gamma_l^* + \psi_{ls}W_l, \tag{8}$$

where U_l, V_l, and W_l are projections of the filament centerline velocity onto $\hat{\mathbf{n}}_l$, $\hat{\mathbf{b}}_l$, and $\hat{\mathbf{t}}_l$, respectively:

$$\frac{8\pi\mu\dot{\gamma}L^4}{E}\frac{\partial\mathbf{x}_l}{\partial t} = U_l\hat{\mathbf{n}}_l + V_l\hat{\mathbf{b}}_l + W_l\hat{\mathbf{t}}_l, \tag{9}$$

$$U_l = \hat{\mathbf{n}}_l\cdot\left\{ \frac{8\pi\mu\dot{\gamma}L^4}{E}\mathbf{U}_0 + \mathbf{u}_l' + [(-c+2)\mathbf{I} + (-2-c)\mathbf{x}_{ls}\mathbf{x}_{ls}]\mathbf{f}_l \right\}, \tag{10}$$

$$V_l = \hat{\mathbf{b}}_l\cdot\left\{ \frac{8\pi\mu\dot{\gamma}L^4}{E}\mathbf{U}_0 + \mathbf{u}_l' + [(-c+2)\mathbf{I} + (-2-c)\mathbf{x}_{ls}\mathbf{x}_{ls}]\mathbf{f}_l \right\}, \tag{11}$$

$$W_l = \hat{\mathbf{t}}_l\cdot\left\{ \frac{8\pi\mu\dot{\gamma}L^4}{E}\mathbf{U}_0 + \mathbf{u}_l' + [(-c+2)\mathbf{I} + (-2-c)\mathbf{x}_{ls}\mathbf{x}_{ls}]\mathbf{f}_l \right\}. \tag{12}$$

The disturbance velocity $\mathbf{u}_l'$ due to hydrodynamic interactions (including both self-interactions and mutual interactions among M filaments) is defined as

$$\mathbf{u}_l' \equiv -K_l - \sum_{k\neq l}^{M} V_{lk}. \tag{13}$$

Instead of using Eq. (12) for W_l, we compute W_l from the normal projection U_l based on the inextensibility condition (by Hou *et al.* [26]) as

$$W_l = \int_0^s U_l\kappa ds' + W_l(s=0), \tag{14}$$

where $W_l(s=0)$ is the tangential velocity at $s=0$. From the complex curvature ψ_l, the filament centerline position can be reconstructed from the Frenet geometric identities as follows. Given a complex curvature ψ_l, the complex vector

$$\omega_l \equiv (\hat{\mathbf{n}}_l + i\hat{\mathbf{b}}_l)\exp(i\phi_l) \tag{15}$$

satisfies the following equations along the filament centerline:

$$\omega_{ls} = -\psi_l\hat{\mathbf{t}}_l, \tag{16}$$

$$\hat{\mathbf{t}}_{ls} = \frac{\psi_l^*\omega_l + \psi_l\omega_l^*}{2}. \tag{17}$$

ω_l and $\hat{\mathbf{t}}_l$ are obtained from integrating Eqs. (16) and (17), and the centerline position is obtained by integrating the tangent vector

$$\mathbf{x}_l = \int_0^s \hat{\mathbf{t}}_l ds' + \mathbf{x}_l(s=0). \tag{18}$$

Substituting Eqs. (10)–(12) into Eq. (6) gives a fourth-order nonlinear integro-differential equation for ψ_l,

$$\eta\frac{\partial \psi_l}{\partial t} = (1+2\delta)(\partial_{ss} + |\psi_l|^2)\{[-\psi_{lss} + (|\psi_l|^2 + T_l)\psi_l] + \omega_l \cdot (\eta \mathbf{U}_0 + \delta \mathbf{u}_l')\} + G_l, \quad (19)$$

with effective viscosity η and filament shape parameter δ defined as

$$\eta \equiv \frac{8\pi\mu\dot{\gamma}L^4}{-cE} = \frac{8\pi\mu\dot{\gamma}L^4}{-\ln(\epsilon^2 e)E}, \quad \delta \equiv \frac{1}{-c} = \frac{1}{-\ln(\epsilon^2 e)}. \quad (20)$$

The force-free boundary conditions expressed in terms of ψ_l are $\psi_l(s=0,1)=\psi_{ls}(s=0,1)=0$. Equation (5) for the line tension can be recast in terms of the complex curvature ψ_l as

$$2T_{lss} - |\psi_l|^2(1+2\delta)T_l = -\left(\int_0^s ds' \frac{\psi_l^* \omega_l + \psi_l \omega_l^*}{2} + \hat{\mathbf{t}}_l(0)\right) \cdot (\eta \mathbf{U}_0 + \delta \mathbf{u}_l')_s - (7-2\delta)(\hat{\mathbf{t}}_{ls} \cdot \hat{\mathbf{t}}_{lsss}) - 6(\hat{\mathbf{t}}_{lss} \cdot \hat{\mathbf{t}}_{lss}). \quad (21)$$

The advantage of the above formulation is that the filament inextensibility condition is exactly satisfied when the filament centerline is reconstructed from the tangent vector. Numerically this means that the filament inextensibility condition is obeyed up to the rounded-off errors without the need for penalty function in the numerical scheme. The end-point tangent vector $\hat{\mathbf{t}}_l(s=0)$ and the filament centerline position $\mathbf{x}_l(s=0)$ are required for constructing the filament centerline. This information is obtained by computing the tangent vector and the filament end point from markers that are convected by the filament velocity from Eq. (9). In the following we outline the implementation of this formulation.

Summary of numerical methods

The integral in Eq. (3) is regularized using the high-order regularization scheme in [20] to achieve consistent asymptotic accuracy of the slender-body formulation of filament dynamics. Equations (19)–(21) are discretized using a second-order time-stepping scheme, and second-order divided differences to discretize the spatial derivatives. An explicit treatment of all terms in Eq. (19) yields a very strict fourth-order stability limit for the time-step size, arising from the high derivatives of ψ_l. Consequently the term ψ_{lssss} is treated implicitly for stability of larger time-step size. Schematically, we write

$$\frac{\partial \psi_l}{\partial t} = \mathbf{F}(\psi_l, \psi_{lssss}) + \mathbf{G}(\psi_l), \quad (22)$$

where the dependence on ψ_{lssss} is to be treated implicitly, and all other terms are to be treated explicitly using a second-order backward differentiation formula. Thus the approximate decomposition reads

$$\frac{1}{2\Delta t}(3\psi_l^{n+1} - 4\psi_l^n + \psi_l^{n-1}) = \mathbf{F}(2\psi_l^n - \psi_l^{n-1}, \psi_{lssss}^{n+1}) + 2\mathbf{G}(\psi_l^n) - \mathbf{G}(\psi_l^{n-1}), \quad (23)$$

where Δt is the time step, and the time at the nth level $t^n = n\Delta t$. For the first time step, before any previous time levels are available, we replace the time discretization above by a first-order Euler step. The spatial discretization in the arc length s is uniform with N intervals of grid space size $h = 1/N$. Second-order divided differences are used to approximate spatial derivatives. The corresponding line tension is then computed by solving Eq. (21) using the same second-order divided differences for spatial discretization. More details on the spatial discretization are provided in [20]. Combining both the temporal and spatial discretizations, we find that this time discretization yields only a first-order constraint for the time-step size; i.e., Δt can be chosen to be proportional to the spatial grid size.

At every time level, the complex vector ω_l and tangent vector $\hat{\mathbf{t}}_l$ are obtained by integrating Eqs. (16) and (17) with moving boundary conditions $\hat{\mathbf{t}}_l(s=0,t)$. As the filament evolves, the boundary condition $\hat{\mathbf{t}}_l(s=0)$ also varies with time. To update $\hat{\mathbf{t}}_l(s=0)$ at the $(n+1)$th level, we use markers that are independent of the filament centerline. The marker velocity is given by Eq. (9) with U_l^n and V_l^n from Eqs. (10) and (11) and W_l^n from Eq. (14), all computed from $\psi_l^n(s)$ and $\omega_l^n(s)$ at the nth time level. The same explicit second-order time-stepping scheme is used to advance the marker positions. Reinitialization of markers is performed if the distance between marker is stretched too much by the velocity field.

The filament shape reconstructed from integrating $\hat{\mathbf{t}}$ along the centerline is always of the same length up to the numerical errors in the integration. No penalty function is needed for enforcing the inextensible condition in the above formulation. The numerical code has been validated against analytic results for a single elastic fiber in prototypical flows such as a linear shear flow and a straining flow. The numerical integrals for hydrodynamic interactions have been validated by checking against analytical results for straight rods in various flow configurations [27].

The rigidity of semiflexible biofilaments (such as microtubules) is in the range $E = 1-30\times10^{-24}$ N m^2 [28]. For filaments of length $L=10$ μm in a fluid of viscosity $\mu = 1$ Pa s and a flow strain rate $\dot{\gamma}=10$ s^{-1}, the effective viscosity is in the range $7500 < \eta < 23\,000$. The typical filament shape parameter is in the range $0.03 \le \delta \le 0.27$. Small values of shape parameter correspond to very slender filaments, for which the hydrodynamic interactions are weak. For the following simulation results we set $\delta \le 0.1$ as we focus on the effects of HIs for slender filaments suitably described by the slender-body theory.

III. TWO FILAMENTS IN LINEAR SHEAR FLOW

In this section we investigate effects of HIs between two elastic filaments immersed in linear shear flow. In particular, we focus on HI-induced change in their buckling dynamics and the filament dispersion in shear flow.

The buckling of a single filament in the plane of shear flow has been well studied [20]. Initially placed at the center of the flow ($y=0$) with an angle $\theta < \pi$ and a small perturbation to the straight shape, the filament slowly rotates to align with the shear flow. The filament experiences compression (decompression) as it rotates toward (past) the vertical axis.

A stiff filament ($\eta=0$) simply rotates to align with the shear flow. For a floppy filament (large η), buckling occurs when sufficient stress is exerted from the fluid during the compression. The filament rotates as it buckles, and eventually straightens out and gradually aligns with the shear (x axis).

Many spatial arrangements of filaments can be considered as initial conditions for simulations of two filaments in shear flow. For force-free filaments the mutual interaction decays with the inverse of filament separation squared [20]. Therefore HIs are most effective when both filaments are in the plane of shear flow. As we seek to elucidate the generic HI effects on filament buckling and the subsequent filament shear dispersion, the two filaments are placed (close to each other) at the same level in the plane of shear flow so that any filament shear dispersion can only result from filament buckling under HIs. Preliminary simulations show that HI effects are most prominent when both filaments buckle at around the same time. In the shear flow this means that both filaments are initially at the same angle with respect to the shear. Therefore, all the simulation results presented in this section start with an initial configuration where both filaments have exactly the same shape and angle so they buckle together and thus maximize the hydrodynamic interactions.

The initial perturbation is explicitly defined in terms of curvature

$$\psi(s) = \delta\psi(s - s^2)^2 \tag{24}$$

for $s \in [0,1]$ and $\delta\psi=10^{-4}$. Two identical filaments are inserted in the xy plane with one centered at (0,0,0) and the other centered at $(d,0,0)$. This initial configuration is not symmetric under the transformation $\mathbf{x}_1 \rightarrow -\mathbf{x}_2$, $\mathbf{x}_2 \rightarrow -\mathbf{x}_1$ [$\mathbf{x}_1$ and $\mathbf{x}_2$ are filament position vectors from $(0,0,d/2)$, the center of two filaments], and the ensuing buckling dynamics will be different between two filaments. At the beginning of the simulations, the angle θ [with respect to the x axis; see Fig. 2(a)] is set to $\theta=0.9936\pi$ for both filaments. This value is chosen so that a noninteracting straight filament will become vertical at $t=49.664$ [20]. Simulations show that hydrodynamic interaction is negligible when filament separation is much larger than five times the filament length.

Finally we remark that perturbations need to be seeded in the simulations for noninteracting filaments to buckle. For interacting filaments with small separation, however, HIs are sufficient to induce filament shape perturbations for buckling under the right conditions. Simulations of interacting filaments show similar filament shear dispersion with or without the small perturbation [Eq. (24)] seeded in the initial conditions.

A. Effect of filament shape parameter δ in shear flow

For the first set of simulations, the initial filament separation is fixed at five times the filament length ($d=5$) with the effective viscosity $\eta=15\,000$, which corresponds to a filament of length $L=5$ μm with $E=10^{-24}$ (or $L=10$ μm with $E=30\times10^{-24}$) in water for a shear rate $\dot{\gamma}=10$ s^{-1}. The filament shape parameter varies from $\delta=0.01$ to $\delta=0.1$, or filament aspect ratio from $\epsilon=10^{-22}$ to $\epsilon=4\times10^{-3}$: the larger the filament aspect ratio (or filament shape parameter δ) is, the more important HIs are to filament dynamics.

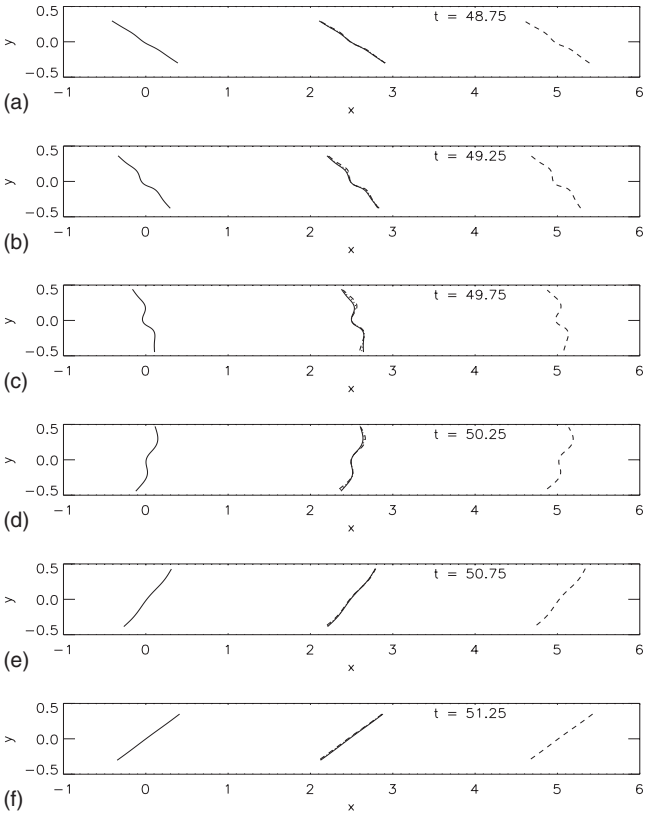

FIG. 2. Buckling instability of two interacting filaments at a distance $d=5$ in a planar shear flow. Effective viscosity $\eta=15\,000$ and filament shape parameter $\delta=0.1$. Both filaments have exactly the same initial shape and angle $\theta(0)=0.9936\pi$. At the center of each panel the two filaments are superimposed for comparison.

Figure 2 shows buckling of two interacting semiflexible filaments in the plane of the shear flow with the initial filament separation $d=5$ and filament shape parameter $\delta=0.1$. For direct comparison, the two filaments are superimposed at the center of each panel. With the initial angle slightly smaller than π, both filaments rotate clockwise in synchrony at this separation. The filament is under compressive stress from the shear flow before it rotates past the y axis. For $\eta=15\,000$ the fluid exerts sufficiently strong compressive stress to induce buckling as filaments rotate past $\theta=3\pi/4$ ($t\sim48.5$). When both filaments are under compression, HIs also induce the most significant difference in the filament shape around $t=49.75$, when the elastic energy $\kappa^2 \equiv \int_0^1 |\psi|^2 ds$ reaches maximum for both filaments; see Figs. 2(c) and 3(a). The dotted line in the figure is the elastic energy of the noninteracting filament, which is exactly the average of the elastic energy for two interacting filaments. This is because the initial conditions are exactly the same for the two interacting filaments, and two filaments rotate and buckle at the same time with the right filament reaching higher curvature than the left. If the sign of perturbation is reversed for both filaments, the left filament will reach higher maximum curvature.

Figure 3(b) plots the elastic energy of the right filament (ordinate) against that of the left filament (abscissa). The

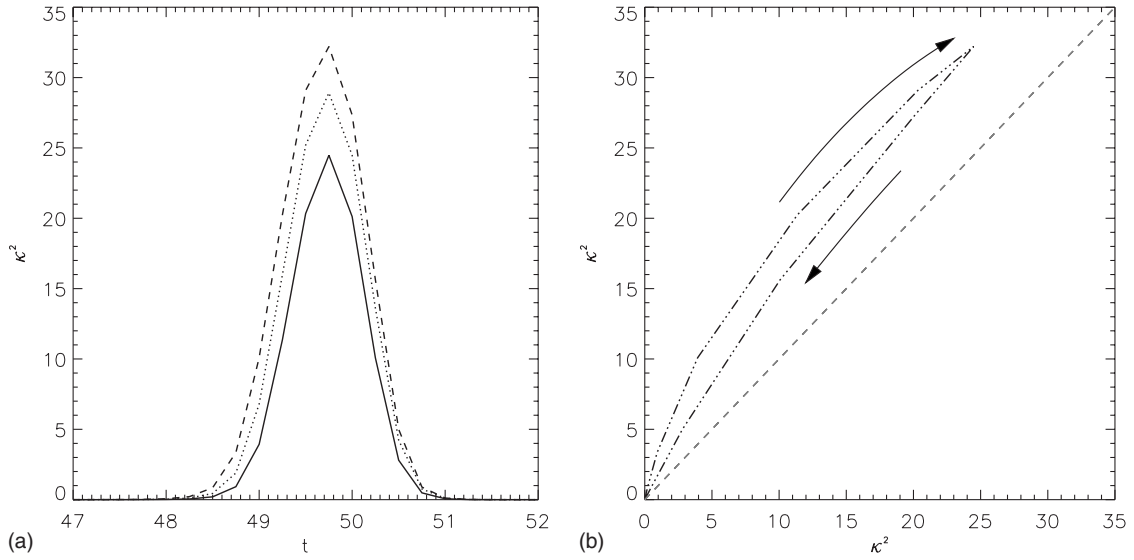

FIG. 3. (a) Elastic energy versus time for interacting filaments in shear flow: solid line for left filament and dashed line for right filament in Fig. 2. The dotted line is for a noninteracting filament with the same initial conditions. (b) Elastic energy of the right filament at $x=5$ (ordinate) versus elastic energy of the left filament at $x=0$ (abscissa). The evolution of the buckling instability follows the arrow. The dashed line is for reference to the evolution of the noninteracting case.

arrows indicate the direction of evolution in terms of the elastic energy of two filaments. The same trend is observed for other values of filament shape parameter as shown in Fig. 4(a). At this separation the two filaments still rotate in synchrony under HIs. Stronger HIs (larger δ) lead to more asymmetric filament shape at the time of buckling ($t \sim 49.75$ for these simulations). After the two filaments buckle and rotate past the vertical axis, they quickly straighten out as in Figs. 2(e) and 2(f).

Another significant consequence of HIs is the filament dispersion in shear flow, which depends on the transverse filament displacement (in the cross-stream direction) defined as $\Delta_y \equiv y_{1c} - y_{2c}$, where y_{lc} is the vertical coordinate of the lth filament center. In the absence of HIs two filaments slowly align with the x axis without any shear dispersion: the transverse filament displacement remains zero, and the filament separation remains constant before and after the buckling. As the interacting filaments rotate and buckle in the shear flow, the transverse displacement Δ_y increases above zero and plateaus to a constant value as both filaments straighten and align with the shear.

From the simulation data it is found that larger HIs (δ) lead to larger transverse filament displacement for $d=5$. Figure 4(b) shows dependence of Δ_y on filament shape parameter via the buckling instability mediated by HIs. The transverse displacement between two filaments is proportional (identical) to the difference in filament translational velocity in shear flow (after nondimensionalization). The difference in translational velocity gives rise to a horizontal filament

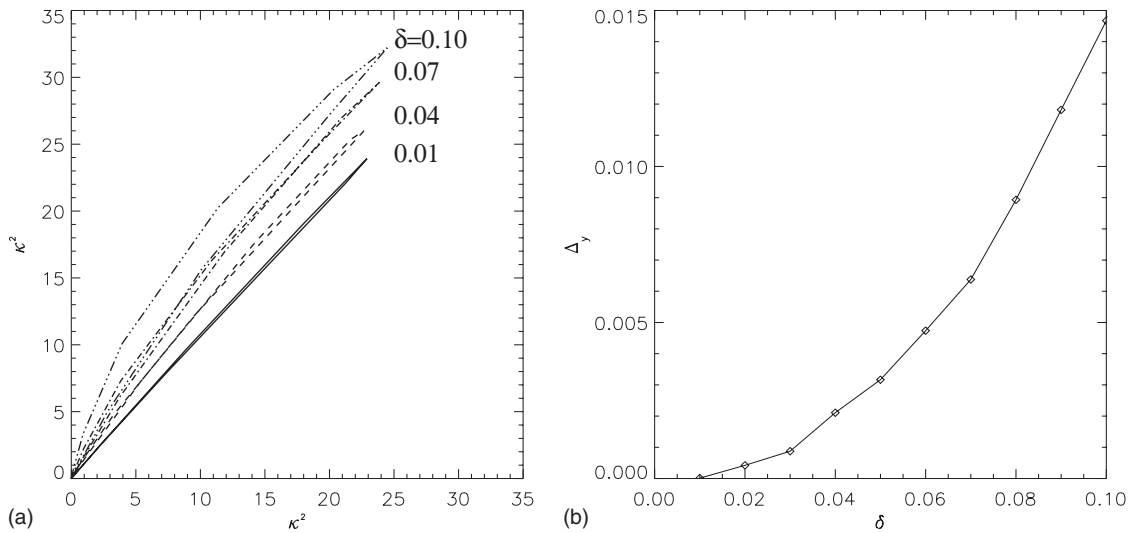

FIG. 4. (a) Elastic energy of the right filament at $x=5$ (ordinate) versus elastic energy of the left filament at $x=0$ (abscissa) for different values of filament shape parameter δ. (b) Dependence of transverse filament displacement Δ_y versus δ.

displacement $\Delta_x = \Delta_y t$, which in turn leads to the filament shear dispersion

$$\Delta(t) \equiv \sqrt{\Delta_x^2 + \Delta_y^2} = \Delta_y \sqrt{t^2 + 1} \to \Delta_y t \quad \text{as} \quad t \to \infty.$$

Therefore, results in Fig. 4(b) suggest that at a fixed initial filament separation, large filament dispersion correlates to large hydrodynamic interaction in the planar shear flow.

B. Effect of initial filament separation in shear flow

More substantial HIs are expected for smaller filament separation because the integral V_{lk} in Eq. (4) vary as $1/|\mathbf{R}_{lk}|^2$. In this subsection we conduct the following set of simulations to examine how the previous results for $d=5$ may vary with initial filament separation. For the following simulation results, filament shape parameter $\delta=0.07$, which corresponds to a filament aspect ratio of $\epsilon \sim 5 \times 10^{-4}$. The initial filament shapes and angles from the previous set of simulations are used, while the initial filament separation d is varied from $d=5$ to $d=1.5$.

Figure 5 shows an example of different HI-induced buckling dynamics for two filaments at a separation $d=2.5$. Figures 5(b)–5(d) show that the filament deformation is almost antisymmetric due to HIs. In this case HIs cause the filament to lose synchrony in their rotation. As illustrated in Fig. 6(a) the right filament rotates faster than the left filament until $t>51$, when the left filament catches up with the right filament [see inset of Fig. 6(a)]. The corresponding evolution of elastic energy for the two filaments is shown in Fig. 6(b). The right filament (dashed line) reaches maximum earlier than the left (solid line). On the other hand, contrary to the case of $d=5$ [also shown in Fig. 6(b)], the left filament deforms more than the right filament, which attains a higher maximum elastic energy at a later time.

For smaller filament separation ($d=1.5$), HIs induce the buckling instability as early as $t \sim 46$. The evolution of filament buckling is demonstrated in Fig. 7. At $t=48.12$ the filaments already undergo significant deformation. After $t=49.37$, half of the filament already straightens out, while the other half is still bent. Both filaments straighten out around $t=52.37$, after when they rotate and gradually align with the shear. The corresponding evolution of the elastic energy is shown as the dash-dotted line in Fig. 8(a). The elastic energy evolutions for $d=2.5$ (dotted line) and $d=5$ (solid line) are also plotted in the figure. For all three curves in Fig. 8(a), the evolution is in the clockwise direction. From these figures we conclude that the asymmetry between the two filaments is most prominent when the filament separation is $d=2.5$. This is also reflected in the transverse filament displacement Δ_y in Fig. 8(b), where Δ_y reaches maximum at $d=2.5$.

The above findings can be understood as follows. When two filaments are far from each other (at a distance greater than five times the filament length), hydrodynamic interaction is negligible and the two filaments rotate in synchrony given the same initial filament shape and angle. When two filaments are in close range of each other, the hydrodynamic interaction causes both filaments to rotate differently. In particular if the initial filament separation is comparable to their

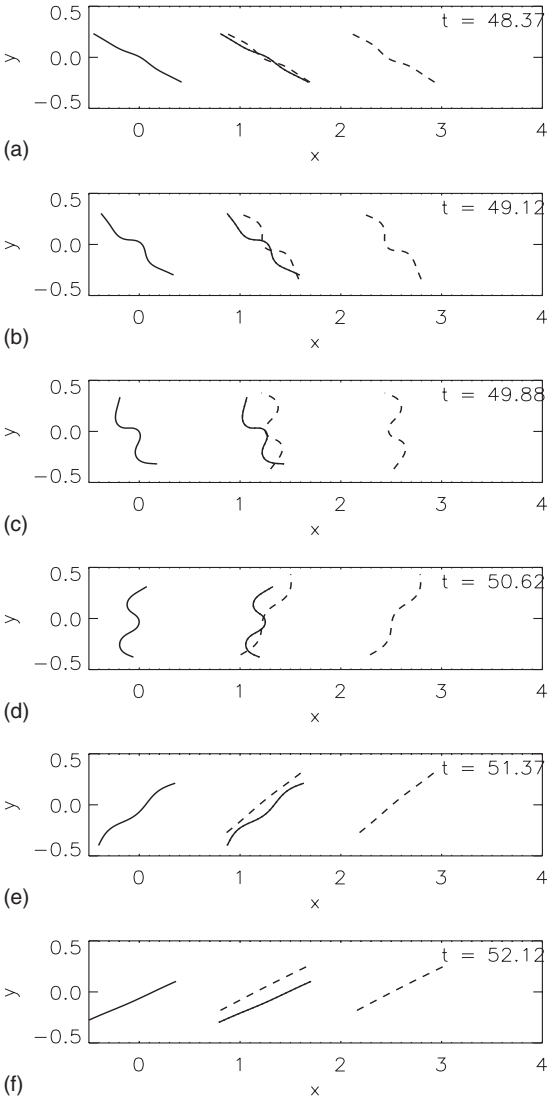

FIG. 5. Buckling instability of two interacting filaments at a separation $d=2.5$ in a planar shear flow. Effective viscosity $\eta = 15\,000$ and filament shape parameter $\delta=0.07$. The same initial conditions are used for both filaments with $\theta(0)=0.9936\pi$. At the center of each panel the two filaments are superimposed for comparison.

length, strong hydrodynamic interaction acts to synchronize the filament rotation. In addition, the shapes of the buckling filaments are (almost) mirror images of each other as clearly demonstrated in Fig. 7. This mirror symmetry (invariant under transformation $\mathbf{x} \to -\mathbf{x}$) is inherent from the linear shear flow. As a result, even though the initial perturbed filament shape (identical for both filaments) does not have the mirror symmetry, strong hydrodynamic interaction enforces this symmetry in the subsequent dynamics. For initial filament separation between the two extreme limits, hydrodynamic interaction is strong enough to induce faster rotation and larger filament deformation than the noninteracting filament, but not enough to enforce the mirror symmetry. Therefore, the buckling dynamics of two filaments at $d=2.5$ shows the most asymmetry, and consequently the largest transverse displacement [solid line in Fig. 8(b)]. The dashed line in Fig.

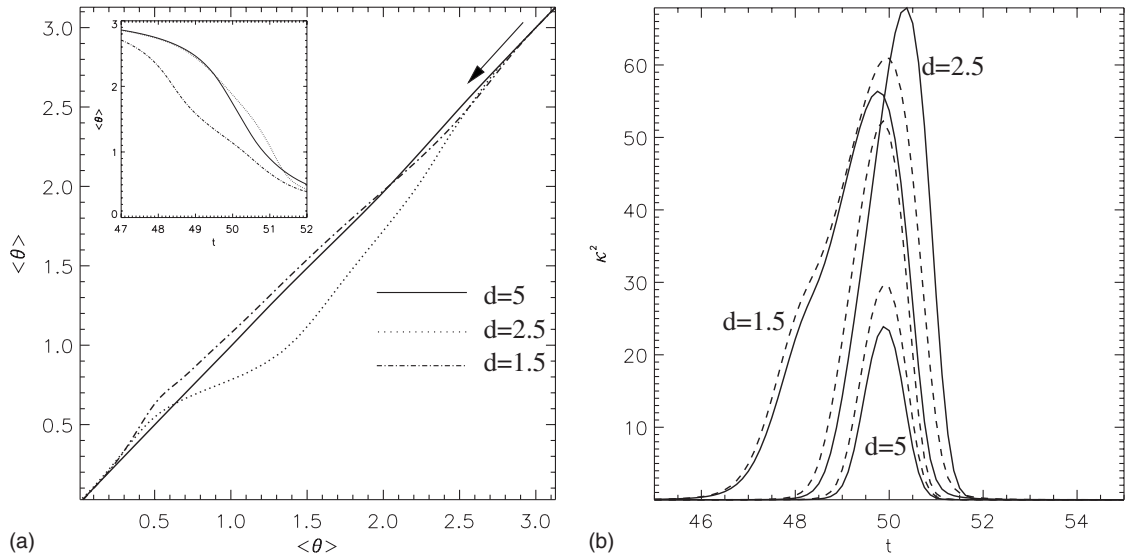

FIG. 6. (a) Evolution of averaged filament angle $\langle\theta\rangle$: right filament (ordinate) versus left filament (abscissa) for initial filament separations $d=5$, $d=2.5$, and $d=1.5$. The arrow indicates the direction of evolution. The inset shows the angle of the left filament versus time. (b) Elastic energy versus time for pairs of filaments at different initial separations with effective viscosity $\eta=15\,000$ and shape parameter $\delta=0.07$. Solid lines are for the left filaments, and dashed lines are for the right filaments.

8(b) is for simulations that start from initial conditions with the mirror symmetry. Similar filament buckling dynamics under HIs are observed for both sets of simulations, and both curves show the general dependence of transverse displacement Δ_y on the filament separation d, even though the exact values depend on the details of the perturbation.

In summary, HIs between two elastic filaments induce different buckling dynamics and filament dispersion (transport) in linear shear flow. Simulation results suggest that filament dispersion is small when the initial filament separation is either too large or too small, and maximum filament dispersion is found for filament separation $d=2.5$ (or two and a half times the filament length). The buckling of filament pair at this distance is found to be most asymmetric, in terms of both average filament curvature evolution and filament rotation.

IV. TWO FILAMENTS IN LINEAR STRAINING FLOW

In this section we elucidate the effects of HIs between two elastic filaments immersed in the plane of a linear straining flow; see Fig. 9(a). As for the cases of linear shear flow, we choose initial configurations to maximize the generic HI effects on the dynamics of filaments in the linear extensional flow. Explicitly, two filaments are placed parallel to the x axis with one on the left (thick solid line) and the other on the right (thick dashed line) of the stagnation point, located at the center of Fig. 9(a). To avoid direct collision as they move toward the stagnation point, the left filament is centered at $(-0.5,-0.03,0)$ and the right is centered at $(0.5,0.03,0)$. The value of 0.03 is chosen so that two filaments do not cross each other when they buckle under HIs around the stagnation point (see Sec. IV B).

The initial conditions for simulation results in this section are perturbed curves [with perturbation given in Eq. (24)] that are invariant under $\mathbf{x}\rightarrow-\mathbf{x}$. The subsequent filament dynamics is expected to be symmetric under the transformation $\mathbf{x}_1\rightarrow-\mathbf{x}_2$, $\mathbf{x}_2\rightarrow-\mathbf{x}_1$ as they are advected by the extensional flow and move along the arrows in Fig. 9(a). This is because both the initial conditions and the straining flow are invariant under this transformation. In the simulations this mirror symmetry is obeyed up to the numerical discretization errors. For unit filament length with 200 grid points for each filament, the filament shapes and trajectories satisfy the mirror symmetry up to errors on the order of $\sim10^{-5}$. For initial conditions with small deviations from such mirror invariance, slight differences in filament trajectories are found but the general filament dynamics is almost identical.

Starting from the initial configuration in Fig. 9(a), two filaments experience more compression as they move closer toward the extensional axis. In this configuration the dynamics of two filaments is always synchronous and spatially invariant under the mirror symmetry. Buckling instability occurs if the effective viscosity is sufficiently large, as in the case of a single filament [22].

For a noninteracting filament on the compressional (x) axis, the critical viscosity for buckling instability is $\eta_c=328$. For $\eta<\eta_c$ the filament does not buckle nor rotate. For $\eta>\eta_c$ the filament buckles, rotates, and aligns with the extensional axis. Once aligned with the extensional axis, the filament moves away from the stagnation point [22]. The complete dynamics of a single filament with supercritical η is the sequence of buckling, rotation, and translation. For a noninteracting filament parallel to the compressional axis at a distance of 0.03 from the compressional axis, the filament experiences compression as it moves toward the extensional axis, and buckles at a critical viscosity lower than 328 (205 for filament at a distance of 0.03).

Different filament dynamics is found from simulations of a pair of interacting filaments approaching the stagnation point. First, HIs cause filaments to buckle at a lower critical

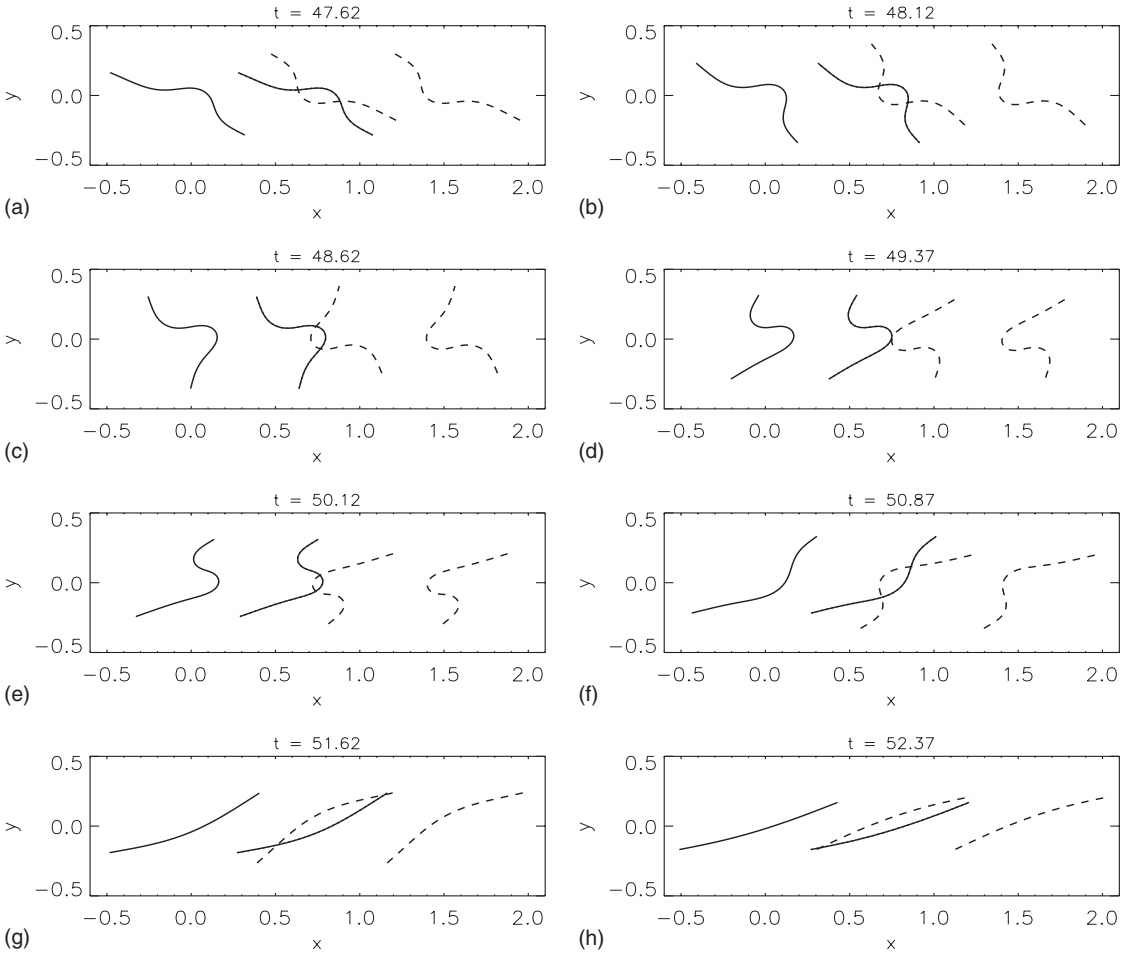

FIG. 7. Buckling instability of two interacting filaments at a distance $d=1.5$ in a planar shear flow with effective viscosity $\eta=15\,000$ and shape parameter $\delta=0.07$. The same initial conditions are used for both filaments with $\theta(0)=0.9936\pi$. At the center of each panel the two filaments are superimposed for comparison.

effective viscosity, which is now a function of filament shape parameter δ as shown in Fig. 9(b). For η below the critical value, filaments with small δ approach the stagnation point without buckling or rotation, and move away from the stagnation point as shown in the lower left inset of Fig. 9(b) (for $\delta=0.01$ and $\eta=190$). For filaments with larger δ (and η still below the critical value), however, the straight filaments rotate under HIs as shown in Fig. 10(a) (for $\delta=0.1$ and $\eta=100$).

Second, for supercritical effective viscosity $\eta>\eta_c$, the two filaments buckle and their elastic energy reaches a maximum [upper right inset of Fig. 9(b)]. The buckling of two interacting filaments around the stagnation point is more complicated than the buckling dynamics of a single filament: The sequence of dynamics for a single filament is found for a pair of interacting filaments only for η slightly above the critical value, as shown in Fig. 10(b) for $\eta=300$ and $\delta=0.1$. Figure 11(a) summarizes the trajectories of filament center from simulations with small to moderate values of η such that filaments rotate to align with the extensional axis.

For η much larger than the critical value, HIs induce significant shape deformation, and the deformed filaments move along the extensional axis without rotation as shown in Fig. 12(a) with $\eta=800$ and $\delta=0.1$. Without HIs, buckling is followed by rotation for a horizontal filament lying on the compressional axis with $\eta=800$ and $\delta=0.1$. Figure 11(b) summarizes the trajectories of filament center with sufficiently large η such that filaments buckle without rotating around the stagnation point. The corresponding elastic energy for buckling filaments with different values of η is plotted versus time in Fig. 12(b).

A. Effect of filament shape parameter δ in extensional flow

Next we examine the shape parameter dependence of buckling dynamics of two filaments as we vary δ from 0.01 to 0.1. $\eta=1000$ is chosen so that filaments buckle for all values of δ. The evolution of the elastic energy versus time is plotted in Fig. 13(a). Detailed buckling dynamics for $\eta=0.01$, 0.02, and 0.03 is illustrated in Fig. 13(b). For all three values of δ filaments start to buckle around $t=2.04$, and the early filament deformation is proportional to δ. For $\delta=0.03$ the filament is more deformed and moves faster than the other two filaments. The filament with $\delta=0.01$ has the least deformation before $t=3.24$. As the $\delta=0.01$ filament moves away from the stagnation point in the V shape, it reaches maximum deformation much later than the other two filaments. The corresponding filament center trajectories also

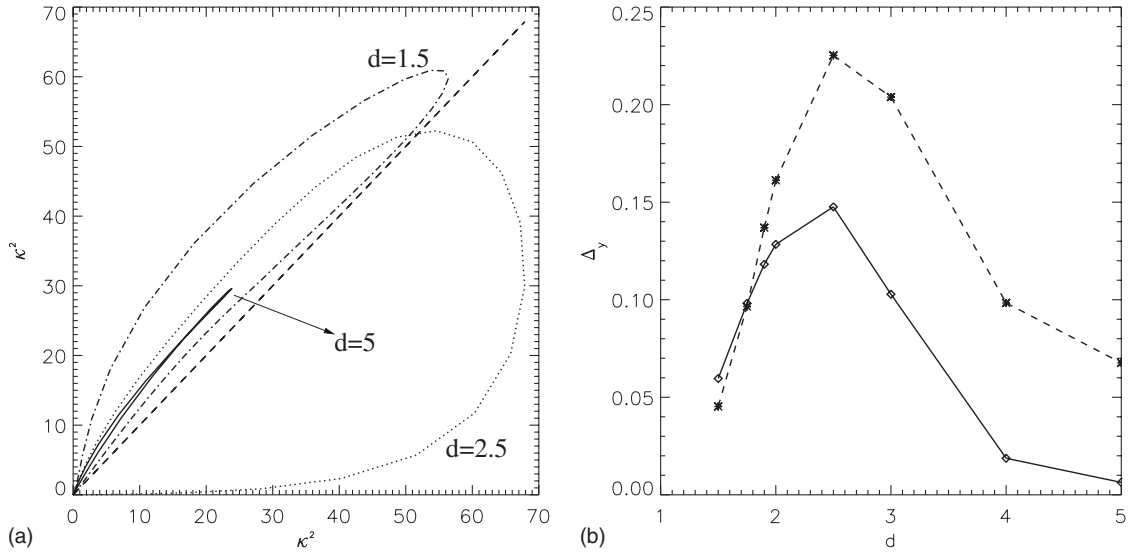

FIG. 8. (a) Elastic energy of the right filament (ordinate) versus elastic energy of the left filament (abscissa) for three initial filament separations. The evolution of the buckling instability follows the clockwise direction. The dashed line is for reference to the evolution of the noninteracting case. (b) Dependence of transverse filament displacement Δ_y versus initial filament separation d. The solid line is for simulations that start from both filaments perturbed by Eq. (24). The dashed line is for simulations that start from initial conditions with the mirror symmetry.

demonstrate the nonmonotonic dependence on shape parameter, and the $\delta=0.01$ filament eventually catches up with the $\delta=0.02$ filament after $t\sim 3.24$. HIs between $\delta=0.01$ filaments induce buckling at a slower rate, and the filament pair reaches maximum curvature farther away from the stagnation point.

B. Buckling filaments in near contact

If filaments are too close to the compressional axis of the extensional flow, their buckling dynamics and rotation around the stagnation point may cause them to be in near contact with each other. An example is shown in Fig. 14(a), where two horizontal filaments are initially centered at $(-0.5,-0.02,0)$ and $(0.5,0.02,0)$. With $\eta=300$ and $\delta=0.1$, two filaments first buckle and then rotate. Around $t=3.64$ the two filaments come into near contact of each other.

Special treatment is required to avoid physical contact and crossing between slender bodies in the slender-body formulation [29]. A strong and very short-range repulsive force often used in the dynamic simulations of rigid fiber suspen-

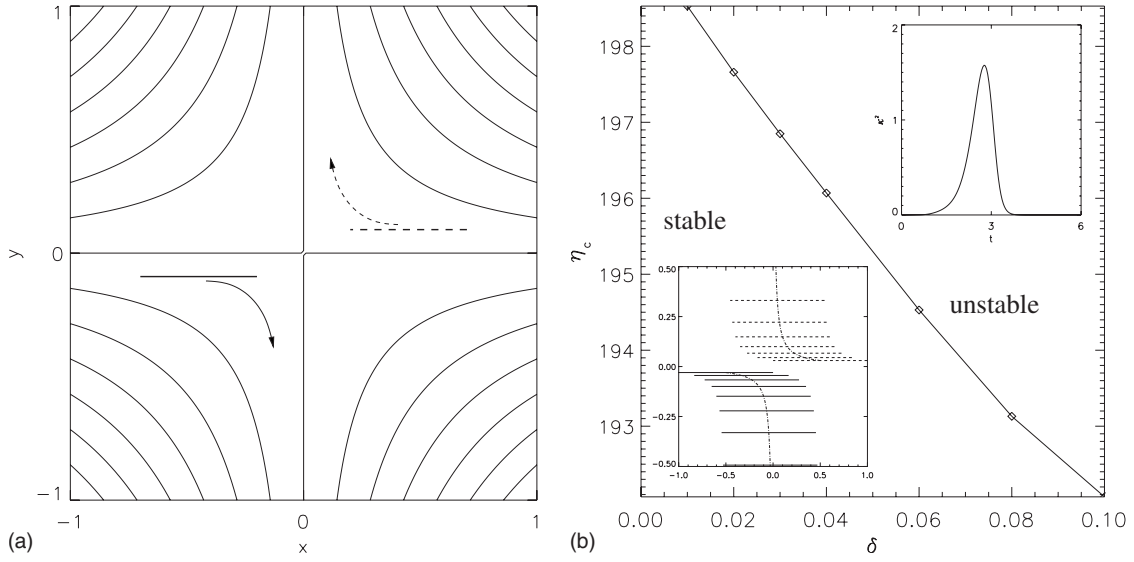

FIG. 9. (a) Illustration of two filaments (thick solid line and thick dashed line) inserted in a linear straining flow $\mathbf{U}_0=(-x,y,0)$. The arrows indicate the flow directions, and the contour lines are the streamlines. (b) Critical value of η for buckling instability of two filaments (parallel to the x axis) around the stagnation point. One filament is moving toward the center from the left at a distance of 0.03 above the x axis and the other at 0.03 below. The inset at the lower left corner is the trajectories of two filaments (with $\eta=200$ and $\delta=0.01$) and their shapes. The inset at the upper right corner is an example of the elastic energy versus time for $\eta=300$ and $\delta=0.1$.

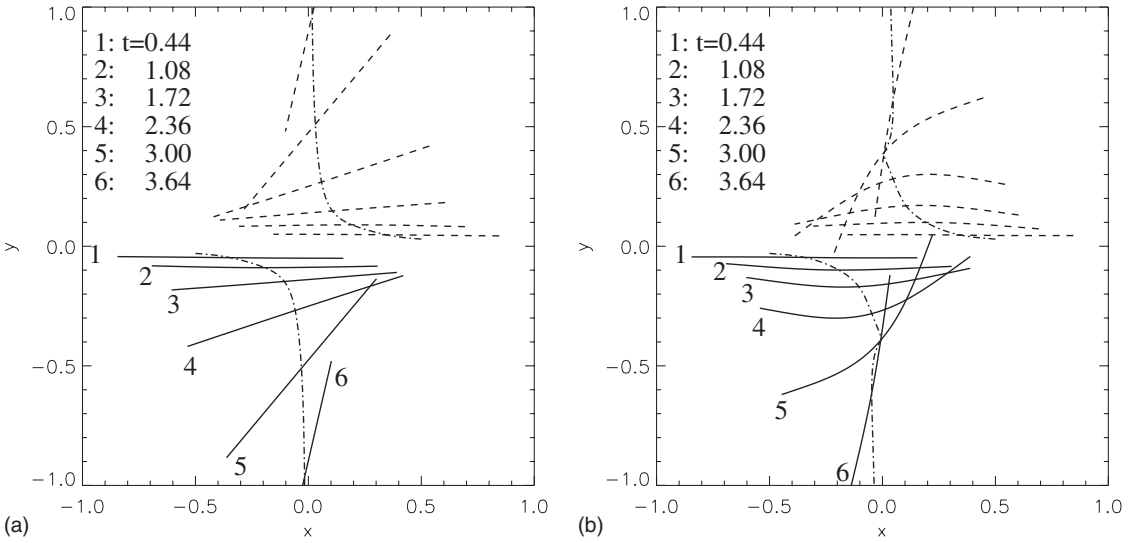

FIG. 10. Trajectories (dash-dotted lines) and shapes of two filaments of unit length with shape parameter $\delta=0.1$ at six different times. The initial configuration is two filaments parallel to the x axis located at $(-0.5,-0.03,0)$ and $(0.5,0.03,0)$. (a) $\eta=100$, and (b) $\eta=300$.

sion is used as an alternative to prevent fiber crossing [30–32]. This repulsive force can be modified for semiflexible filaments as follows:

$$\mathbf{F}_l^R(s) = \pm a_0 \frac{\tau e^{-\tau h_{lk}(s)}}{1 - e^{-\tau h_{lk}(s)}} \hat{\mathbf{n}}_l, \tag{25}$$

where $h_{lk}(s)$ is the shortest distance between two filaments at a given point on the lth filament, and proper signs are chosen to denote the repulsive direction.

Without the short-range repulsive force, the two filaments in Fig. 14(a) come into physical contact and the slender-body formulation breaks down right after $t=3.64$. Adding the repulsive force with $a_0=10^{-4}$ and $\tau=10^3$ in the simulation, the two filaments slide next to each other after $t=3.64$, rotate and align with the extensional axis, and diverge from the stagnation point after $t=4.28$. Figure 14(b) shows the corresponding evolution of the elastic energy (dashed line). In comparison with the elastic energy for $d=0.03$ (solid line), HIs suppress filament deformation when they are in close range of each other, an effect also found in the case of viscous drops [6]. Further numerical investigation on the buckling filaments in close range shows that the repulsive force with $a_0=10^{-4}$ and $\tau=10^3$ in Eq. (25) fails to keep the buckling filaments from crossing each other in some cases. Different values for a_0 and τ can be used to prevent filament crossing.

V. CONCLUSION

The effects of HIs on the buckling dynamics of a pair of semiflexible inextensible filaments in two simple linear flows

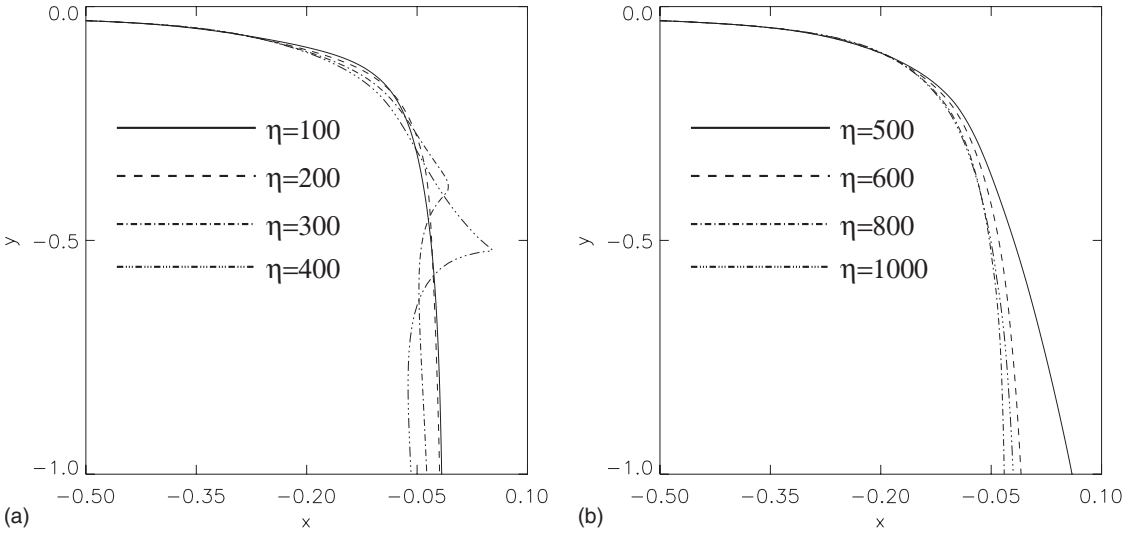

FIG. 11. Trajectories of the center of left filament with $\delta=0.1$ for different values of η. The right filament trajectories are mirror images with respect to the origin. (a) Moderate η where the filament buckles mildly for $\eta > \eta_c$ and rotates as it leaves the stagnation point (Fig. 10). (b) Large η where the filament deforms significantly and does not rotate as it leaves the stagnation point [Fig. 12(a)].

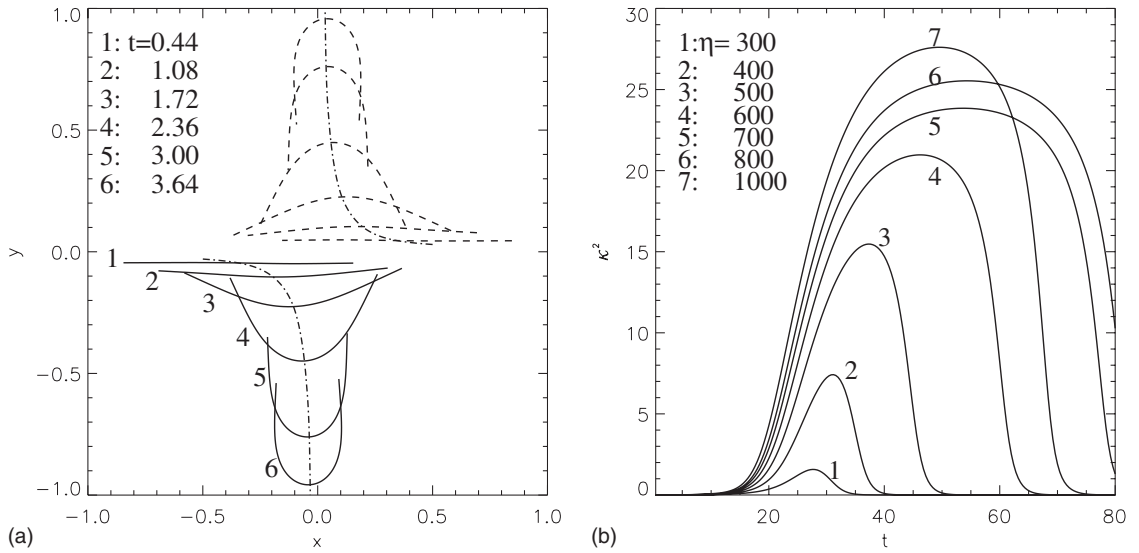

FIG. 12. (a) Trajectories (dash-dotted lines) and shapes of filaments with $\delta=0.1$ and $\eta=1000$ at six different times. The initial configuration is two filaments parallel to the x axis located at $(-0.5,-0.03,0)$ and (0.5,0.03,0). (b) Elastic energy versus time for η from 300 to 1000.

are reported in this paper. The nonlocal slender-body formulation for interacting filaments immersed in Stokes flow is utilized to describe the dynamics. Specific initial conditions are used in the numerical simulations to elucidate the various aspects of HIs.

For a pair of identical filaments (same shape, angle, and bending rigidity) lying at the center of shear flow with an initial separation d, we find HIs change the filament rotation in nontrivial fashions. First, HIs induce filaments to rotate earlier than noninteracting filaments. Second, simulations show that filament rotation is synchronous when the filament separation is large (with negligible HIs) or small (very strong HIs). For an intermediate filament separation $d=2.5$ filament rotation is out of sync, with the right filament completing the rotation earlier than the left one for the given initial conditions. Third, HIs also induce nontrivial filament shear dispersion in shear flow: without HIs the filament shear dispersion is zero for the given initial conditions. Filament shear dispersion first increases with decreasing filament separation, attains a maximum at $d=2.5$ when the loss of synchrony in filament dynamics is the greatest, and decreases when the filaments are synchronized again by strong HIs at short filament separation.

We have also simulated the dynamics of a pair of filaments initially centered at $(-49.664,1,0)$ and (0,0,0), both with an angle $\theta=0.9936\pi$. The top, left filament translates horizontally toward the right at a dimensionless velocity of 1. Two filaments are closest to each other at $t=49.664$ when the top filament center reaches (0,1,0). As both filaments buckle around $t=49.664$, HIs induce most differences in

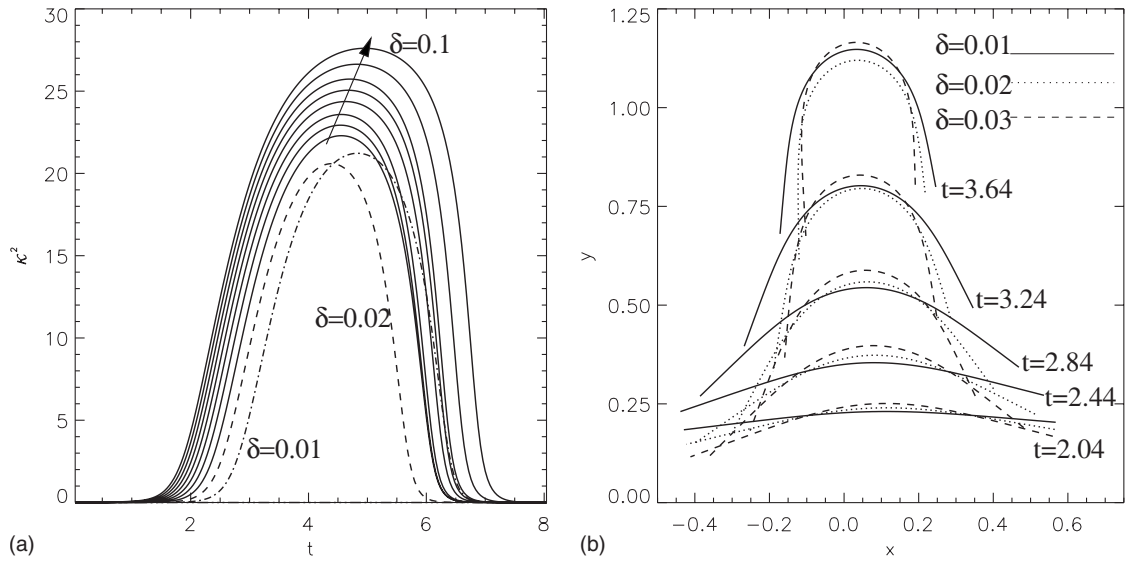

FIG. 13. δ dependence of buckling dynamics around the stagnation point. Effective viscosity $\eta=1000$ and two filaments of unit length are initially located at $(-0.5,-0.03,0)$ and (0.5,0.03,0). (a) Evolution of elastic energy for $\delta=0.01$ to $\delta=0.1$ with an increment of 0.01 between curves. (b) Filament shapes at different times for $\delta=0.01$, $\delta=0.02$, and $\delta=0.03$.

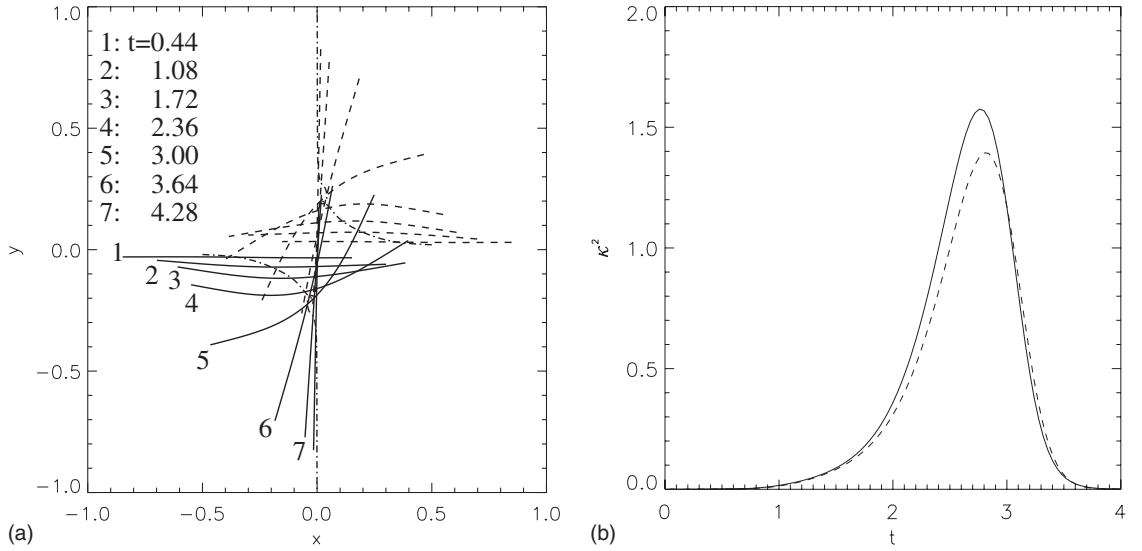

FIG. 14. (a) Buckling filaments with $\eta=300$, $\delta=0.1$, and $d=0.02$. The two filaments come into near contact around $t=3.64$. Repulsive force is needed to prevent filament crossing in the simulation. (b) Elastic energies for different initial displacements from the compressional (x) axis: solid line is for a displacement of 0.03 and dashed line is for a displacement of 0.02. $\eta=300$ and $\delta=0.1$ for both cases.

shape deformation. As in the previous cases, the consequence of filament buckling under HIs is an increase in filament dispersion after both filaments straighten out and align with the shear. However, for this configuration, the final transverse displacement for $\delta=0.1$ is $\Delta_y \sim 1.01$, an increase of only 0.01. Therefore we conclude that HIs have little impact on the shear dispersion of filaments moving toward each other at this vertical separation. For smaller vertical separation, two filaments may come into physical contact around $t=49$.

For a pair of filaments in the extensional flow, a special initial condition is chosen so that (1) two filaments would approach the stagnation point from equal distance, and (2) the subsequent dynamics retains the mirror symmetry up to numerical discretization errors. HIs reduce the threshold in bending rigidity for buckling instability in this configuration. For stiff filaments converging to the stagnation point in the flow, strong HIs can induce rotation. For moderately floppy filaments, HIs induce both buckling and rotation of filaments, much similar to the buckling dynamics of a single filament around the stagnation point. For very floppy filaments, HIs induce strong filament deformation and the highly deformed filaments diverge from the center without rotation.

We have also shown that two filaments come into near contact as they buckle around the stagnation point. The slender-body formulation breaks down if two filaments are in physical contact, which occurs when two filaments are very close to the compressional axis as suggested in Fig. 14(a). A short-range repulsive force is found to be able to keep two filaments apart only for certain ranges of effective viscosity and shape parameter. More detailed investigation is required to ensure that the slender-body formulation remains consistent in these cases. Once we have a better treatment of the repulsive force for buckling filaments in near contact, we will investigate how HIs affect the transport of short filaments (less than 1 μm) in a cellular flow in the presence of thermal fluctuations, which may lead to filament tumbling [19] and coiling [33].

An ongoing project is to examine how macroscopic properties of semiflexible filament suspension correlate to HIs effects on the buckling dynamics of a pair filaments summarized in this paper. We are now working on incorporating the smooth-particle mesh Ewald (SPME) scheme for fast computation of the interaction integral V_{lk} into the nonlocal formulation for multifilaments in a periodic domain. We aim to simulate more than hundreds of interacting semiflexible filaments, and these results will be useful for constructing and validating the modeling of HIs in the framework of kinetic theory for complex filament flows in the dilute or semidilute limit. For example, the integral kernel of filament interaction [34] may be consistently constructed based on the findings presented in this paper.

ACKNOWLEDGMENTS

The author acknowledges invaluable help from Jerome T. Morrison, and helpful discussion with M. J. Shelley, P. Vlahovska, and J. Bławzdziewicz. The author also acknowledges support of NSF under Grants No. DMS-0708977 and No. DMS-0420590 for the computing cluster at NJIT.

[1] D. Saintillan, E. Darve, and E. S. G. Shaqfeh, Phys. Fluids **17**, 033301 (2005).
[2] D. Saintillan and M. J. Shelley, Phys. Rev. Lett. **99**, 058102 (2007).
[3] A. Sokolov, I. S. Aranson, J. O. Kessler, and R. E. Goldstein, Phys. Rev. Lett. **98**, 158102 (2007).
[4] D. Saintillan and M. J. Shelley, Phys. Rev. Lett. **100**, 178103 (2008).
[5] M. Baron, J. Bławzdziewicz, and E. Wajnryb, Phys. Rev. Lett. **100**, 174502 (2008).
[6] M. Loewenberg and E. J. Hinch, J. Fluid Mech. **338**, 299 (1997).
[7] V. Kantsler, E. Segre, and V. Steinberg, EPL **82**, 58005 (2008).
[8] C. H. Wiggins, Math. Methods Appl. Sci. **24**, 1325 (2001).
[9] L. J. Fauci and R. H. Dillon, Annu. Rev. Fluid Mech. **38**, 371 (2006).
[10] R. H. Dillon, L. J. Fauci, C. Omoto, and X. Yang, Ann. N.Y. Acad. Sci. **1101**, 494 (2007).
[11] X. Yang, R. H. Dillon, and L. J. Fauci, Bull. Math. Biol. **70**, 1192 (2008).
[12] D. Riveline, C. H. Wiggins, R. E. Goldstein, and A. Ott, Phys. Rev. E **56**, R1330 (1997).
[13] L. Dreyfus, J. Baudry, M. L. Roper, M. Fermigier, H. A. Stone, and J. Bibette, Nature (London) **437**, 862 (2005).
[14] C. Goubault, P. Jop, M. Fermigier, J. Baudry, E. Bertrand, and J. Bibette, Phys. Rev. Lett. **91**, 260802 (2003).
[15] A. Koenig, P. Hebraud, C. Gosse, R. Dreyfus, J. Baudry, E. Bertrand, and J. Bibette, Phys. Rev. Lett. **95**, 128301 (2005).
[16] R. K. Doot, H. Hess, and V. Vogel, Soft Matter **3**, 349 (2007).
[17] C. H. Wiggins, D. Riveline, A. Ott, and R. E. Goldstein, Biophys. J. **74**, 1043 (1998).
[18] R. E. Goldstein, T. R. Powers, and C. H. Wiggins, Phys. Rev. Lett. **80**, 5232 (1998).
[19] T. Munk, O. Hallatschek, C. H. Wiggins, and E. Frey, Phys. Rev. E **74**, 041911 (2006).
[20] A.-K. Tornberg and M. Shelley, J. Comput. Phys. **196**, 8 (2004).
[21] I. Llopis, I. Pagonabarraga, M. Cosentino Lagomarsino, and C. P. Lowe, Phys. Rev. E **76**, 061901 (2007).
[22] Y.-N. Young and M. J. Shelley, Phys. Rev. Lett. **99**, 058303 (2007).
[23] M. C. Lagomarsino, I. Pagonabarraga, and C. P. Lowe, Phys. Rev. Lett. **94**, 148104 (2005).
[24] K. Nakayama, H. Segur, and M. Wadati, Phys. Rev. Lett. **69**, 2603 (1992).
[25] R. E. Goldstein and S. A. Langer, Phys. Rev. Lett. **75**, 1094 (1995).
[26] T. Hou, J. Lowengrub, and M. J. Shelley, J. Comput. Phys. **169**, 302 (2001).
[27] Y.-N. Young (unpublished).
[28] J. Howard, *Mechanics of Motor Proteins and the Cytoskeleton* (Sinauer Associates, Sunderlad, MA, 2001).
[29] O. G. Harlen, R. R. Sundararajakumar, and D. L. Koch, J. Fluid Mech. **388**, 355 (1999).
[30] L. J. Durlofsky and J. F. Brady, J. Fluid Mech. **200**, 39 (1989).
[31] J. E. Butler and E. S. G. Shaqfeh, J. Fluid Mech. **468**, 205 (2002).
[32] P. R. Nott and J. F. Brady, J. Fluid Mech. **275**, 157 (1994).
[33] C. M. Schroeder, R. E. Teixeira, E. S. G. Shaqfeh, and S. Chu, Macromolecules **38**, 1967 (2005).
[34] I. S. Aranson, A. Sokolov, J. O. Kessler, and R. E. Goldstein, Phys. Rev. E **75**, 040901(R) (2007).